A resonant squid-inspired robot unlocks biological propulsive efficiency

Thierry Bujard,[1] Francesco Giorgio-Serchi [1,2], Gabriel D. Weymouth [1,3*]

[1] Engineering and Physical Sciences, University of Southampton, Southampton, UK
[2] School of Engineering, University of Edinburgh, Edinburgh, UK
[3] Data-Centric Engineering Programme, Alan Turing Institute, London, UK

*To whom correspondence should be addressed; E-mail: G.D.Weymouth@soton.ac.uk

Elasticity has been linked to the remarkable propulsive efficiency of pulse-jet animals such as the squid and jellyfish, but the underlying dynamics have not been quantified nor utilized in any robotic system. This work identifies the pulse-jet propulsion mode utilized by these animals as a coupled mass-spring-mass oscillator, enabling the design of a new flexible self-propelled robot. We use this system to experimentally demonstrate that resonance greatly benefits pulse-jet swimming speed and efficiency, and the robot's optimal cost of transport is found to match that of the most efficient biological swimmers in nature, such as the jellyfish *Aurelia aurita*. The robot also exhibits a preferred Strouhal number for efficient swimming, thereby bridging the gap between pulse-jet propulsion and established findings in efficient fish swimming. Extensions of the current robotic framework to larger amplitude oscillations could combine resonance effects with optimal vortex formation to further increase propulsive performance and potentially outperform biological swimmers altogether.

Introduction

Resonance exploitation in elastic components is a ubiquitous and powerful idea which can enhance performance in domains as diverse as harvesting environmental energy and singing soprano (*1–3*). In terrestrial walking (*4*), jumping (*5*) and even terrestrial snake propulsion (*6*) exploiting mechanical resonance has been used to significantly increase propulsive efficiency. For example, passive dynamic walkers (*4*), non-actuated systems capable of performing bipedal locomotion by exploiting resonant dynamics, laid the groundwork for under-actuated robotic walkers an order of magnitude more efficient than their fully controlled predecessors (*7*).

Much less work has focused on resonance exploitation for biologically-inspired underwater robots and vehicles, despite evidence that this is used by animals. The use of flexible materials has been studied extensively in biological flapping foil propulsion, such as fish swimming (*8*) and insect flight (*9*). Here, the efficiency increase has been associated with the synchronization of the vortex shedding and the undulating body deformations, both from self-induced vortices (*10*) and upstream wakes induced by obstacles or other swimmers (*11, 12*). However, the majority of engineering studies simplify the complex body mechanics of a swimming fish down to a single flexible plate, and more complete robotic systems, such as the high frequency swimming robot of (*13*), exploit flexibility in their fins at most and have not focused on resonance. Considering a different biological propulsive model may offer more opportunities to exploit resonance for underwater robotics.

A variety of marine life such as jellyfish, octopuses, salps, shellfish and squids use periodic or pulse-jetting as a form of locomotion, Figure 1(A). Pulse-jetting entails the cyclic expansion and contraction of a hollow cavity of the specimen's body, which in turn drives the ingestion and expulsion of ambient fluid. Pulse-jetting organisms are known to excel in short-distance, predatory swimming, in addition to sustained propulsion (*14*). Fluid dynamics modeling and
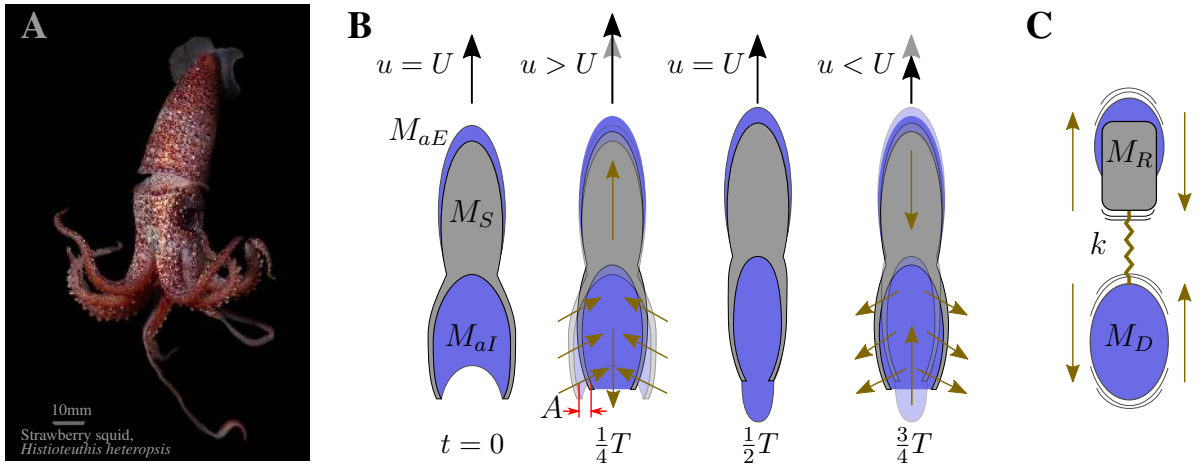
Figure 1: Conceptual framework for resonant squid-like propulsion. (A) A strawberry squid is one of many animals which utilize pulse-jet swimming; image credit Paul Caiger © Woods Hole Oceanographic Institution. (B) Schematic of the simplified pulse-jet swimming mode used in this work having body deformation period $T = 1/f$, amplitude A, and instantaneous swimming speed u which varies around the average speed U. The grey body is the swimmer of mass M_S, which flexibly contracts (from $t/T = 0$ to $\frac{1}{2}$) and expands ($t/T = \frac{1}{2}$ to 1) its body cavity to force fluid in and out with added mass M_{aI}. The inline acceleration of the body also accelerates some external flow with added mass M_{aE}. (C) This fundamental mode of motion is equivalent to a linear mass-spring-mass oscillator. The driving mass $M_D = M_{aI}$, and is always out of phase with the reaction mass $M_R = M_S + M_{aE}$, while the stiffness k is determined by the body flexibility and geometry.

experiments have shown that the vortex ring and size-change generated by a pulse-jet produce a propulsive thrust well in excess of a steady jet (*15, 16*). These findings have spurred the development of a range of pulse-jet and size-changing robotic vehicles (*17–21*), even including a micro-robotic version of a juvenile jellyfish with variable kinematics (*22*). However, none of these robots or any other in the literature exploit resonance, relying instead on direct actuation or explosive one-time jets.

Much the same as resonance exploitation in walking and flapping animals, the nature and geometric arrangement of muscle fibres in a squid mantle (*23*) hints that elastic energy may play a role in their propulsion (*24, 25*). Similarly, the jellyfish *Polyorchis penicillatus* was found to swim with a frequency related to the stiffness of its bell (*26*), suggesting that this enables the

species to maximize the use of elastic energy storage to power the refilling stage of the cycle and thus minimize metabolic energy consumption. Experimental studies of a flexible cavity showed that stiffness did indeed impact the thrust and shape of the resulting vortex rings (*27,28*). While these experiments were performed on a fixed platform, numerical simulations of a flexible bell-shaped boundary driven with simplified jellyfish-like kinematics suggest large amplitudes can be achieved at resonant frequencies in a vacuum (*29*) and that this should translate to faster swimming speeds (*30*).

Despite the indication that resonance is somehow being exploited in biological pulse-jetting, no resonant squid-like robots have been developed to date. A key challenge is that none of these biological or experimental studies identified the fundamental resonant mechanism at play, quantifying the impact of the structural and fluid dynamics on the resonance of active swimming. Understanding the governing oscillator dynamics has been crucial for the design of resonant walking and flapping robotics, and a similar understanding is required for pulse-jetting. In this study we achieve the goal of a highly efficient resonant robotic swimmer inspired by pulse-jetting animals such as the squid and jellyfish using three major contributions: (i) we identify the leading mechanical and hydrodynamic parameters of pulse-jet swimming and use them to formulate a simple analytic dynamical swimming model (ii) we use this model to develop a flexible jetting robot with simple periodic actuation capable of resonance when constrained and when freely swimming, and (iii) we show the measured performance of the robot validates our simple model of pulse-jet resonance and enables the robot to achieve self-propelled speeds comparable to the most efficient swimmers in nature.

Results

Resonant pulse-jet propulsion   Identifying the leading-order dynamic characteristics of a pulse-jet swimmer is crucial to determine its potential resonant frequency and exploit resonance

in a pulse-jet robot. Abstracting across species which utilize pulse-jet propulsion, such as the squid in Fig 1(A), we develop a model swimmer which is roughly a truncated ellipsoid in shape and uses radial oscillations at a frequency f and amplitude A to pump fluid in and out of an internal cavity to propel itself at an average speed U, Fig. 1(B). The details of the ingestion and ejection of fluid vary among animals, but we will consider the simplest case where the fluid is drawn in and out through the same opening, as with jellyfish. Similarly, animals use different muscle actuation schedules to pump the fluid, but we will limit our study to simple harmonic body deformation which efficiently produces thrust proportional to the fluid jet velocity squared (*15, 31*). As the jet velocity U_j is proportional to Af, increasing amplitude through resonance will increase thrust and swimming speed for a given biological or robotic actuation force.

The contraction and expansion of the cavity accelerates the internal fluid radially and axially. The radial contributions cancel due to symmetry but the axial accelerations accumulate to produce a large driving force which accelerates the body axially in the opposite direction. In other words, the internal fluid inertia acts as the driving mass M_D of the axial oscillations, the flexible cavity acts as a spring with stiffness k, and the swimmer's inertia M_R reacts to the driving motion out of phase. Therefore, the fundamental oscillation mode of a flexible pulse-jetting swimmer is equivalent to a coupled mass-spring-mass system, sketched Fig. 1(C). As suggested from Fig. 1 the driving mass equals the added-mass of the internal cavity flow M_{aI}, and the reaction mass is the sum of the solid swimmer's mass M_S and the external fluid added-mass M_{aE}.

This linear oscillator model is elaborated in the Materials and Methods section, and the resulting undamped natural frequencies are

$$f_C = \frac{1}{2\pi}\sqrt{\frac{k}{M_D}}\,, \quad f_F = f_C\sqrt{1 + \frac{M_D}{M_R}} \;>\; f_C$$

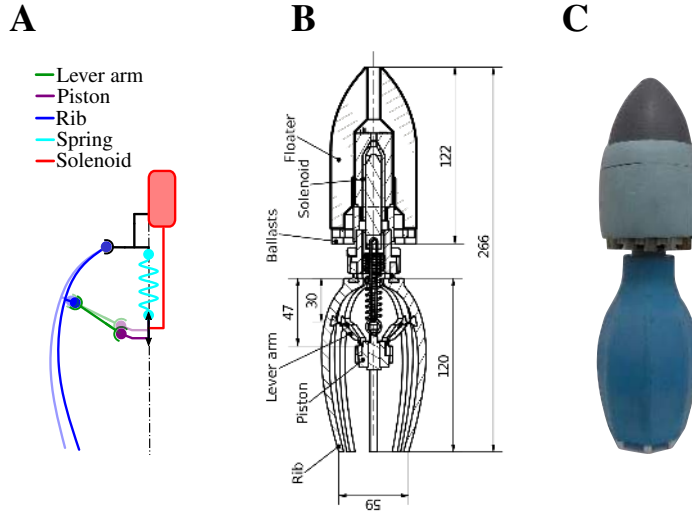where f_C is the natural frequency when the swimmer is *constrained* from reacting inline, and

5

Figure 2: The flexible bio-inspired resonant robot. (A) Linkage schematic of the cavity actuation system (B) Principle elements of the design shown in cross-section. Dimensions given in mm. (C) The built prototype with the membrane mounted (blue).

f_F is the natural frequency during *free* self-propelled swimming. For a given force, actuating the system near this frequency will maximize the deflection amplitude A, and therefore thrust and swimming speed. The peak amplitude of a damped linear oscillator occurs when forced at frequency $f = f_n\sqrt{1 - \zeta^2}$ where f_n is the natural frequency and ζ is the damping ratio of the system, proportional to the relative energy lost per cycle.

Vehicle Design   The prototype robot employed in this study consists of an umbrella-like apparatus with eight ribs arranged axisymmetrically and driven into radial expansion by a linear actuator, Fig. 2. The geometry of the cavity is defined by a membrane stretched over the ribs and pre-tensioned to prevent localized wrinkling. The piston is linked to a linear tension spring aligned with the axis of the vehicle which balances the inward force of the stretched membrane. Together, the spring and the membrane determine the equilibrium position of the cavity and the elasticity of the structure.

The excitation force is provided by a solenoid actuator mounted along the axis of symmetry

of the vehicle in a frontal compartment. The actuator cyclically compresses the cavity in the range of 2.0 to 17.0 Hz thus driving out a jet of fluid. The actuator is powered externally via a tether and is surrounded by low-density foam to ensure the robot is neutrally buoyant and that its center of buoyancy is above its center of mass, making the robot naturally stable when upright in water. This eliminates the need for any control system and focuses the study on steady propulsion, but extensions to manoeuvring vehicles are straightforward (*32*). The complete vehicle has a dry mass of $M_S = 0.380\ kg$ and overall length of $L = 0.266\ m$. A qualitative demonstration of the robot freely swimming is show in Movie 1.

The flexible robot was tested in multiple arrangements shown in Fig. 3, allowing the properties of the dynamic model to be determined experimentally as detailed in the Materials and Methods section. Free-vibration tests in water using the stationary set-up in Fig. 3(A) measured the robot's constrained natural frequency as $f_C = 5.73\ Hz$ and damping ratio as $\zeta = 0.15$. The constrained rig was also used to measure the effective stiffness of the cavity as $k = 1.60\ kN/m$. These measurements determine the cavity flow's added mass underwater to be $M_{aI} = 1.23\ kg$, completely overwhelming the inertia of the vibrating ribs and membrane. This is consistent with analytic estimates of M_{aI} reported in the Materials and Methods section, and emphasizes the critical role added mass plays in the oscillator dynamics. Finally, the external added-mass was roughly estimated using the analytic value for a prolate spheroid with the same length and minor semi-axis dimension of $4\ cm$ giving $M_{aE} = 0.15\ kg$ (*33*), around 40% of the dry mass. Substitution of these inertia factors into the frequency equation predicts $f_F \approx 10\ Hz$ when freely swimming, though this ignores the influence of the tether on the dynamics.

Robot performance   To demonstrate successful resonance exploitation, we quantify the robot's free swimming performance using three standard metrics; the swimming speed U, the quasi-
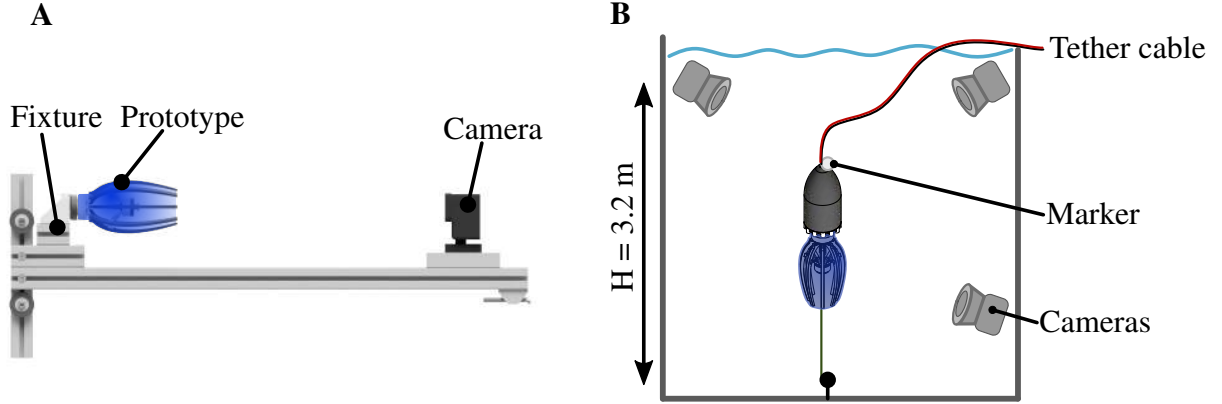
7

Figure 3: Experimental test arrangements. (A) The stationary setup used for the effective stiffness measurements, the free oscillation tests and the forced oscillation tests. (B) Free-swimming setup used for the buoyancy-driven and actuated swimming tests.

propulsive efficiency η, and the mechanical cost of transport COT, defined as

$$\eta = \frac{RU}{P} , \quad \mathrm{COT} = \frac{P}{gM_S U}$$

where P is the power supplied by the actuator, R is the robot's fluid drag (resistance) when traveling at speed U, and g is the acceleration of gravity.

An actuation frequency sweep was performed on the robot when it was constrained from axial motion underwater as in Fig. 3(A) to determine the powering characteristics. Fig. 4 quantifies the measured deformation amplitude in terms of the Stroke Ratio commonly used in pulse-jet studies (15), and defined as $\mathrm{SR} = L_{jet}/D$, where D is the jet aperture diameter and $L_{jet} = 4V_{jet}/(\pi D^2)$ is a length scale of the ejected fluid volume V_{jet}. The supplemental notebook S1 shows $\mathrm{SR} \propto A/D$ with the proportionality constant determined by the cavity geometry and deformation mode. Fig. 4 shows the stroke ratio peaks when excited just below the undamped natural frequency as expected. The phase measurements also show the expected behaviour, but have an uncertainty proportional to the frequency due to the constant frame rate of the motion capture data.

These measurements are used to fit a dynamical model of the actuated cavity deformation,

detailed in the Materials and Methods section. Fig. 4 indicates the model fits the data extremely well and the modelled damping ratio is $\zeta = 0.29 \pm 0.01$, indicating that solenoid actuator's losses are somewhat hindering the potential for resonance exploitation. This model allows the power P delivered by the actuator to the robot to be determined, and is used in the free swimming tests. Fig. 4 shows the powering has a fairly small uncertainty other than at low frequency due to the non-linear forcing supplied by the solenoid actuator.

Finally, the drag $R(U)$ was measured using the motion capture set-up of Fig. 3(B). The vehicle was given a positive net buoyancy by removing one or more ballast weights, released to float upward, and the terminal velocity U was measured. As the drag and known buoyancy balance when U is steady, this determines $R(U)$, given in Fig. S6.

The performance of the robot during self propelled swimming was also measured with motion capture sketched in Fig. 3(B) as detailed in the Materials and Methods section. The self-propelled swimming results for speed, efficiency and cost of transport are shown in Fig. 5. The highest speed of 0.98 L/s occurs at 9 Hz. The peak efficiency of 56% and minimum cost of transport of 0.087 are measured at $f = 7.5\ Hz$, although the entire range from 6-10 Hz have high efficiency and nearly identical COT. The confidence in the COT $\sim P/U$ is lowest at low frequency because the confidence in P is lowest in that region and the swimming speeds U are very small.

Discussion

A dynamic model for resonant swimming was developed and tested with a flexible biologically-inspired swimming robot, resulting in a clear increase in performance near its natural frequency. This observed speed peak at 9 Hz is lower than the 10 Hz natural frequency estimate due to the expected influence of damping and neglecting the influence of the tether on the robot's free swimming dynamics. The tether is also responsible for a portion of the fairly high vehicle
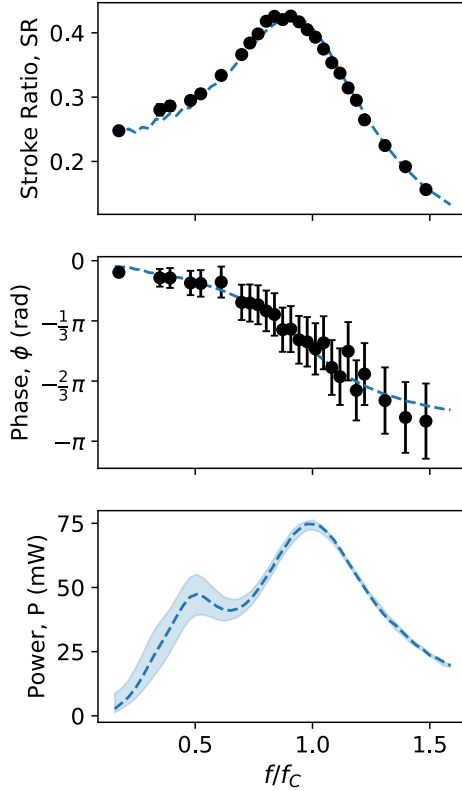
Figure 4: Actuated frequency sweep results when constraining the robot from axial motion. The excitation frequency is scaled by the natural frequency and the oscillation amplitude is reported in terms of the stroke ratio (*15*). Black dots and bars show the median and 95% confidence interval (CI) of the measurements ($n \geq 51$ cycles), and the blue line and shaded area are the median and 95% CI of the dynamical model after fitting to the measurements.

drag, Fig. S6, meaning an un-tethered vehicle with the same powering could see further speed improvements.

The tests performed with this flexible prototype provide a useful comparison to biological and other robotic swimmers. Table 1 shows measurements done by (*15, 34, 36*) on squids and jellyfish. Care has to be taken in comparing across studies as efficiency and cost metrics vary, and swimming routines of certain organisms may account for a combination of jetting and paddling (e.g. in jellyfish), but the performance of the swimming prototype comfortably falls within the range of marine species. In particular, the minimum cost of transport for the robot
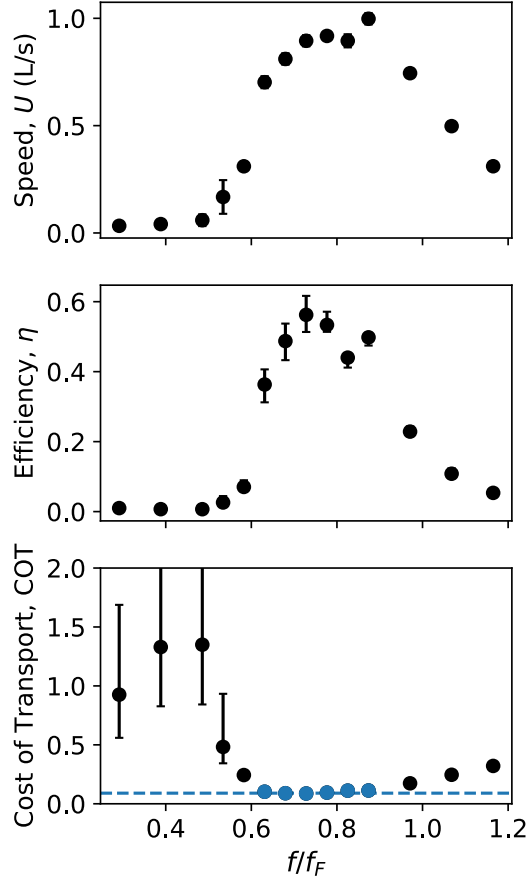
10

Figure 5: Free-swimming robot performance versus scaled actuation frequency. Points and bars are the median and 95% CI from the measurements ($n \geq 44$ cycles) and dynamical model. The colored points intersecting the dashed line at $\textbf{COT} = 0.09$ show constant St behaviour in Fig. 6.

at resonance $\mathrm{COT} = 0.087$ falls into the $0.03 - 0.09$ range reported for the moon jellyfish *Aurelia aurita*, which outperform any other swimming animal and any other engineered vehicle (ground, air, or sea) other than extremely large slow-moving ships on this metric (*41*).

For the range of $f = 6 - 10 \; Hz$ leading up to the natural frequency estimate $f_F \approx 10 \; Hz$, Fig. 5 shows that the robot achieves a nearly uniform low cost of transport, around $\mathrm{COT} \approx 0.09$. A uniform COT is significant because it means the power P and speed U are proportional for efficient swimming, in stark contrast to the typical behavior $P \propto U^3$ in fluid propulsion.

Table 1: Non-dimensional characteristics of marine species compared to the current resonant propulsion prototype. Symbol SR and L_b stand for stroke ratio and body length.

	Unit	This study	squid[1]	jellyfish[2]	jellyfish[3]	squid[4]	fish[5]	fish[6] CFD	fish[7] robot
U	L_b/s	0.04 - 0.98	0.3 - 2.06	0.7 - 4.0	0.16 - 0.66	-	-	-	-
SR	-	0.24 - 0.42	5.5 - 61.8	-	-	-	-	-	-
fL/U	-	8.3 - 72.9	0.6 - 2.5	-	4.5 - 9.3	-	-	-	-
U_j/U	-	1.35 - 11.5	1.5 - 4.5	-	-	-	-	-	-
η	-[8]	0.01 - 0.56	0.38 - 0.44	0.1 - 0.55	-	-	-	0.39 - 0.46	0.32
COT	-[9]	0.087 - 1.3	-	-	0.03 - 0.09	0.5 - 0.65	0.09 - 0.7	-	-

[1] data for adult squid from (34).

[2] data from (35), with U given in bell diameter/s, which is maintained here since the studied species have a low aspect ratio in the range $\sim 0.5 - 2$. Although the stroke ratio is not explicitly given, it is stated that some species display stroke ratios < 4, and others use higher strokes.

[3] data for jellyfish from (36).

[4] data for squids from (36) based on original measurements from (37).

[5] data for fish from (38).

[6] estimates of η using a CFD (computational fluid dynamics) simulation of carangiform and anguilliform fish swimming from (39).

[7] data for robotic fish from (40).

[8] this study, (39) and (40) use quasi-propulsive efficiency; (34) use whole cycle hydrodynamic efficiency; (35) use Froude efficiency.

[9] this study reports the mechanical COT, whereas the biological studies report metabolic COT. In addition, we have scaled (36) by g to obtain a non-dimensional metric.

Resonant propulsion is able to avoid this scaling because increasing the frequency near the natural frequency increases the amplitude A without increasing the required actuation force. Since the jet velocity U_j is proportional to Af, this is equivalent to stating that increasing f up to resonance increases jet velocity and thrust faster than linearly, with the result that the $P \sim U$ until the resonant peak is crossed.

The vehicle displays a constant Strouhal number $\text{St} = 2Af/U \approx 0.15$ in this region as well, Fig. 6, connecting pulse-jet swimming to the extensive literature indicating a Strouhal number preference in efficient flapping foil propulsion. While counter examples such as the high-frequency swimming robot of (13) suggest the relationship between St and maximum
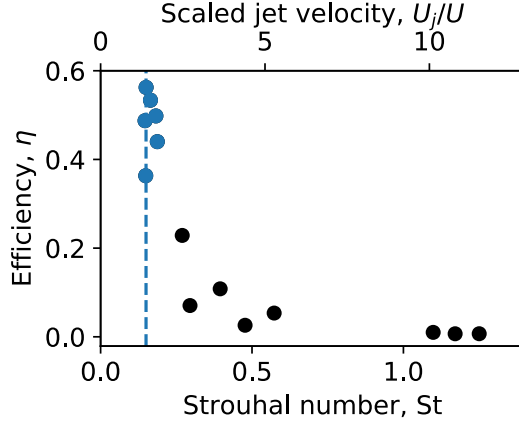
Figure 6: Quasi-propulsive efficiency as a function of Strouhal number $\mathrm{St} = 2Af/U$ or jet velocity U_j scaled by swimming speed U. Median values are shown. The points near the dashed line at $\mathrm{St} = 0.15$ show uniform cost of transport in Fig. 5.

efficiency is not completely understood, flapping animals with the same ratio of propulsor size to body size tend to share the same optimal Strouhal number $0.2< \mathrm{St} <0.4$ (*42, 43*), and the current pulse-jet robot has an optimal St as well. As the Strouhal number for the flexible robot does not go under the optimal value, there is a maximal swimming speed attainable for a given jet velocity U_j, and the limiting ratio for this vehicle is around $U/U_j \approx 70\%$.

Table 1 shows that pulse-jet animals such as jellyfish and squid use a wide range of deformation amplitudes $(5 < \mathrm{SR} < 62)$ when swimming (*34*), while the current robot is limited to $\mathrm{SR} < 0.5$ due to the synthetic membrane. Tensile testing of the mantle tissue of squids during escape jetting indicates fairly low viscoelastic damping, having an hysteresis between 15-25% in the elastic energy variation between the expulsion and refill phase (*24, 25*). This suggests that viscous damping of the mantle remains low even during large amplitude jetting, meaning squid tissue could exploit resonance at significantly higher stroke ratios. Instead, the likely limiting factor in exploiting resonance is the viscous fluid losses due to ingestion and ejection of large volumes of water. This increased fluid damping means animals using a stroke ratio much greater than 10 are likely sacrificing the chance to benefit from resonance in favour of

rocket-like manoeuvring, i.e. large body accelerations driven by large mass ejections.

Greatly reducing the size of the swimmer down to the micrometric range would also enhance fluid damping by lowering the Reynolds number to $Re = UL/\nu \sim 1$, where $\nu \approx 10^{-6} \frac{m^2}{s}$ is the kinematic viscosity of water. However, pulse-jet swimmers in nature range from less than a centimeter in size up to tens of meters (*44*), thus operating from $1 < Re < 10^8$, and MEMS devices have been designed to exploit resonance even at the micrometric scale (*2*), giving some reason to hope that resonant robotic swimmers could also be designed for use across this range.

Finally, previous bio-mechanical studies on pulse-jetting find that additional fluid thrust is measured when using a stroke ratio around 4 to create an optimal fluid vortex, and many animals are observed to swim near that range (*15*). As this is still a modest stroke ratio, these animals could be benefiting from mechanical resonance in addition to optimal vortex formation. Increasing the achievable stroke ratio of the resonant robotic systems to match biological levels in the future should allow it to exploit these jet vortex dynamics, further improving performance. Even with this limitation, the current flexible prototype achieves unprecedented biological levels of efficiency and is a powerful demonstrator of the potential to exploit resonance efficiently in biological swimmers and biologically-inspired robotics.

Materials and Methods

Stationary tests   The results reported in Tab. S2 and Fig. 4 are obtained from tests performed with the vehicle held stationary, Fig. 3(A). A camera is used to film the jet exit plane of the vehicle to record the position of the rib tips in free and forced oscillations, Fig. S3.

Free vibration tests in air and water are used to measure the natural frequency and damping in the expansion/contraction mode. The free vibration was excited using a wire to apply a fixed displacement to the piston to contract the ribs, and then cutting the wire. Four tests in each fluid were executed, and an example of the traces from two of the tests are shown in Fig. S4.

A damped harmonic was fit to each measurement signal and used to determine their frequency and damping. Measurement statistics are reported in Tab. S2.

A similar test configuration is used to measure the stiffness k_{eff} of the piston. The piston displacement under prescribed loading was measured four times; before and after the free vibration tests, and while loading and unloading the spring. Fig. S5 shows the characteristic is linear but shows a slight hysteresis. A linear fit of all the data gave $k_{eff} = 11.35 kN/m$ stiffness.

The actuated frequency sweep uses the same fixed rig shown in Fig. 3(A), but the motion is achieved by driving the piston with the solenoid actuator. The actuator was prescribed a harmonic voltage with fixed amplitude and variable frequency and the rib displacement is recorded as before. An LED added in the camera frame marks the start of the excitation period, allowing the response phase to be determined although the constant frame rate of 24 Hz lowers the confidence in these phase measurements, Fig. 4. After the initial ramp into the steady oscillator dynamics was removed, the remaining cycles ($n \geq 51$ actuation cycles were obtained for all cases) where used to determine the coefficients for the forced oscillator model, as discussed below.

Free-swimming tests   The results reported for Fig. 5 are obtained from tests performed with the vehicle moving freely under water, Fig. 3(B). An underwater motion capture system comprised of four cameras arranged around a 3.2m square with a sample rate of 100 Hz was set up in the middle of an extremely large ($130m$x$6m$x$3.5m$) tank and is used to measure the ascent velocity. System calibration indicated a 0.15% error in relative position measurement.

The self-propelled tests are performed with the prototype neutrally buoyant and allowing it to ascend the water column exclusively under the effect of the thrust generated by its own actuation. The large 3.2m vertical distance allowed the robot to achieve steady swimming for more than 400 measurement images and $n \geq 44$ actuation cycles in every test. The $0.025, 0.5$

and 0.975 quantiles of the steady data were used to determined the median and 95% confidence interval of the speed U. The robot was reset at the same starting position for each test with a five minute window between tests to allow the water to come to rest.

The robot drag curve $R(U)$ is determined by measuring the steady terminal velocity of the prototype as it ascends the water column under a known buoyancy force without actuation. As in the actuated swimming, at least 400 measurements were made per test and the median and 95% CI are shown in Fig. S6. These results are used to estimate a drag coefficient $C_d = R/(\frac{1}{2}\rho U^2 a_f) = 1.13$ where a_f is the frontal area. The relatively high C_d values for such a slender body suggest significant resistance due to towing the tether.

Free-swimming demonstration The qualitative demonstration of the robot's swimming ability shown in Movie 1 was not recorded in the test conditions described above. To simplify video capture, the demo used a much smaller tank with the vehicle close to a viewing window and weights were added to make the robot negatively buoyant so the robot would descend unassisted.

Free-vibration model Application of Newton's second law to the undamped unforced mass-spring-mass oscillator in Fig. 1(C) gives

$$M_R \ddot{x}_R = -k(x_R - x_D), \qquad M_D \ddot{x}_D = -k(x_D - x_R)$$

where x_D, x_R are the axial displacements of the driving and reactive masses relative to their centroid. During free-vibration, both displacements will be harmonic with the same frequency f_F and so the coupled system becomes

$$\begin{bmatrix} k - (2\pi f_F)^2 M_R & -k \\ -k & k - (2\pi f_F)^2 M_D \end{bmatrix} \begin{bmatrix} x_R \\ x_D \end{bmatrix} = \begin{bmatrix} 0 \\ 0 \end{bmatrix}$$

As such the determinant of this matrix must be zero and the free-swimming natural frequency must satisfy $(2\pi f_F)^2 = k(M_R + M_D)/(M_R M_D)$. When the vehicle is constrained, $x_D = 0$ and so the constrained frequency must satisfy $(2\pi f_C)^2 M_R = k$.

Next, we assume the driving inertia M_D is due to the internal added mass M_{aI} acting at the center of action of the cavity deformation mode. For small rigid body oscillations of the ribs around the pivot (see Fig. 2(A,B)) the center of action is two thirds of the length of the cavity $2/3L_c = l_{aI} = 80\ mm$, and using the lever arm from the pivot to the push rod $l_{pivot} = 30mm$ we arrive at the reported effective stiffness of the robot $k = k_{eff}l_{pivot}^2/l_{aI}^2 = 1.6\ kN/m$.

The free-vibration measurements in water in Tab. S2 and this value of k give the reported $M_D = 1.23\ kg$ in water. We can independently estimate M_{aI} by assuming the axial flow speed v inside the cavity is the primary contribution to the fluid kinetic energy K_E. In that case

$$K_E = \frac{1}{2}M_{aI}\dot{A}^2 \approx \frac{1}{2}\rho \int v^2 dv$$

where $\dot{A}$ is the rate of change of deformation amplitude. As detailed in the python notebook S1, substituting the robot's cavity shape and the assumed linear deformation mode determines the speed v and predicts $M_{aI} = 1.2\ kg$, in good agreement with the free-vibration measurements.

Forced oscillation model The efficiency and cost of transport metric require accurate modelling of the actuated cavity dynamics so the oscillation amplitude and phase and the delivered mechanical power can be established on the free swimming robot as a function of the actuation frequency. Power consumption measured via a current meter is not equivalent to delivered power because of the significant dissipation and losses in the tether and solenoid. This issue is amplified by the low power draw of the robot, decreasing the signal to noise ratio of such a measurement.

Instead, the self-propelled power used in Fig. 5 is determined by calibrating a simple forced

oscillator model to the constrained frequency sweep data in Fig. 4

$$\ddot{x} + 2\zeta\omega_n\dot{x} + \omega_n^2 x = \frac{F(x - x_0, V)}{M_{eff}}$$

where x is the spring compression, $\omega_n = 2\pi f_C$, $M_{eff} = M_D$ for the constrained tests, and F is the actuator force which is a known nonlinear function of the supplied voltage V and the solenoid's position relative to it's rest position x_0, Fig. S7. As the voltage is known, the only free parameters are the rest position and damping, which are tightly constrained by the measurements to $x_0 = 5.1 \pm 0.3\ mm$ and $\zeta = 0.29 \pm 0.01$. As shown in Fig. 4, the model gives an excellent fit to the data with extremely small uncertainty in the oscillation amplitude and phase. There is moderate uncertainty in the cycle-averaged delivered power $P = \frac{1}{T}\int_0^T F\dot{x}dt$ at low frequency because of the nonlinear forcing supplied by the solenoid, but this doesn't impact the confidence near resonance where the response is essentially linear.

As the free swimming linear model is still a single mode oscillator, it is sufficient to adjust the mass M_{eff} in the forced oscillator model above such that $\omega_n = 2\pi f_F$. The powering system is unchanged when releasing the robot for free swimming, and therefore we use the same median and confidence bounds on x_0 and ζ for free-swimming. The predicted SR and P are shown in Fig. S8.

Supplementary Materials and Methods

Python notebook S1: Cavity geometry calculations.

Tab S2: Constrained Free Vibration measurements

Fig S3: Constrained test image example.

Fig S4: Free-vibration example results.

Fig S5: Force vs displacement measurements and the linear fit.

Fig S6: Terminal velocity resistance measurements and quadratic fit.

Fig S7: Actuator force as a function of relative position and voltage.

Fig S8: Forced oscillator model results.

References

1. G. W. Taylor, J. R. Burns, S. Kammann, W. B. Powers, T. R. Welsh, *The energy harvesting eel: a small subsurface ocean/river power generator*, *IEEE journal of oceanic engineering* **26**, 539 (2001).

2. C. Wu, *et al.*, *A spring-based resonance coupling for hugely enhancing the performance of triboelectric nanogenerators for harvesting low-frequency vibration energy*, *Nano Energy* **32**, 287 (2017).

3. E. Joliveau, J. Smith, J. Wolfe, *Tuning of vocal tract resonance by sopranos*, *Nature* **427**, 116 (2004).

4. S. Collins, A. Ruina, R. Tedrake, M. Wisse, *Efficient Bipedal Robots Based on Passive-Dynamic Walkers*, *Science* **307**, 1082 (2005).

5. D. W. Haldane, M. M. Plecnik, J. K. Yim, R. S. Fearing, *Robotic vertical jumping agility via series-elastic power modulation*, *Science Robotics* **1** (2016).

6. A. Kakogawa, S. Jeon, S. Ma, *Stiffness Design of a Resonance-Based Planar Snake Robot With Parallel Elastic Actuators*, *IEEE Robotics and Automation Letters* **3**, 1284 (2018).

7. F. L. Moro, N. G. Tsagarakis, D. G. Caldwell, *Walking in the resonance with the COMAN robot with trajectories based on human kinematic motion primitives (kMPs)*, *Autonomous Robots* **36**, 331 (2014).

8. F. Paraz, L. Shouveiler, C. Eloy, *Thrust generation by a heaving flexible foil: Resonance, nonlinearities, and optimality*, *Physics of Fluids* **28**, 011903 (2016).

9. S. Ramananarivo, R. Godoy-Diana, B. Thiria, *Rather than resonance, flapping wing flyers may play on aerodynamics to improve performance*, *Proceedings of the National Academy of Sciences* **108**, 5964 (2011).

10. M. J. Shelley, J. Zhang, *Flapping and bending bodies interacting with fluid flows*, *Annual Review of Fluid Mechanics* **43**, 449 (2011).

11. J. C. Liao, D. N. Beal, G. V. Lauder, M. S. Triantafyllou, *Fish exploiting vortices decrease muscle activity*, *Science* **302**, 1566 (2003).

12. A. D. Becker, H. Masoud, J. W. Newbolt, M. Shelley, L. Ristroph, *Hydrodynamic schooling of flapping swimmers*, *Nature communications* **6**, 8514 (2015).

13. J. Zhu, *et al.*, *Tuna robotics: A high-frequency experimental platform exploring the performance space of swimming fishes*, *Science Robotics* **4** (2019).

14. R. K. O'Dor, D. M. Webber, *Invertebrate athletes: trade-offs between transport efficiency and power density in cephalopod evolution*, *Journal of Experimental Biology* **160**, 93 (1991).

15. J. O. Dabiri, *Optimal vortex formation as a unifying principle in biological propulsion*, *Annual review of fluid mechanics* **41**, 17 (2009).

16. M. S. Triantafyllou, G. D. Weymouth, J. Miao, *Biomimetic Survival Hydrodynamics and Flow Sensing*, *Annual Review of Fluid Mechanics* **48**, 1 (2016).

17. L. Ruiz, R. Whittlesey, J. Dabiri, *Vortex-enhanced propulsion*, *Journal of Fluid Mechanics* **668**, 5 (2011).

18. A. Moslemi, P. Krueger, *Propulsive efficiency of a biomorphic pulsed-jet underwater vehicle*, *Bioinspiration & Biomimetics* **5**, 1 (2010).

19. M. Krieg, K. Mohseni, *Thrust characterization of a bio-inspired vortex ring generator for locomotion of underwater robots*, *IEEE Journal of Oceanic Engineering* **33** (2008).

20. G. D. Weymouth, V. Subramaniam, M. S. Triantafyllou, *Ultra-fast escape maneuver of an octopus-inspired robot*, *Bioinspir. Biomim.* **10**, 016016 (2015).

21. F. Giorgio-Serchi, A. K. Lidtke, G. D. Weymouth, *A Soft Aquatic Actuator for Unsteady Peak Power Amplification*, *IEEE/ASME Transactions on Mechatronics* **23**, 2968 (2018).

22. Z. Ren, W. Hu, X. Dong, M. Sitti, *Multi-functional soft-bodied jellyfish-like swimming*, *Nature Communications* **10**, 2703 (2019).

23. M. Krieg, K. Mohseni, *New perspective on collagen fibers in the squid mantle*, *Journal of Morphology* **273**, 586 (2012).

24. J. M. Gosline, R. E. Shadwick, *The role of elastic energy storage mechanisms in swimming: an analysis of mantle elasticity in escape jetting in squid, Loligo opalescens*, *Canadian Journal of Zoology* **61**, 1421 (1983).

25. P. S. Macgillavray, E. J. Anderson, G. M. Wright, M. E. Demont, *Structure and mechanics of the squid mantle*, *Journal of Experimental Biology* **202**, 683 (1999).

26. M. E. DEMONT, J. M. GOSLINE, *Mechanics of jet propulsion in the hydromedusan jellyfish, Polyorchis pexicillatus: I. Mechanical properties of the locomotor structure*, *Journal of experimental Biology* **134**, 313 (1988).

27. A. A. Villanueva, K. J. Marut, T. Michael, S. Priya, *Biomimetic autonomous robot inspired by the Cyanea capillata (Cyro)*, *Bioinspiration & Biomimetics* **8(4)**, e98310 (2013).

28. A. Villanueva, P. Vlachos, S. Priya, *Flexible Margin Kinematics and Vortex Formation of Aurelia aurita and Robojelly*, *PLoS-ONE* **9(6)**, e98310 (2014).

29. W. Hsieh, T. Chen, *On the resonance analysis for compliant bionic jellyfishes*, *Science China Technological Sciences* **53**, 2976 (2010).

30. A. Hoover, L. Miller, *A numerical study of the benefits of driving jellyfish bells at their natural frequency*, *Journal of theoretical biology* **374**, 13 (2015).

31. M. Krieg, K. Mohseni, *Modelling circulation, impulse and kinetic energy of starting jets with non-zero radial velocity*, *Journal of Fluid Mechanics* **719**, 488 (2013).

32. T. Wang, A. K. Lidtke, F. Giorgio-Serchi, G. D. Weymouth, *2019 2nd IEEE International Conference on Soft Robotics (RoboSoft)* (2019), pp. 186–191.

33. A. I. Korotkin, *Added masses of ship structures*, vol. 88 (Springer Science & Business Media, 2008).

34. E. J. Anderson, M. A. Grosenbaugh, *Jet flow in steadily swimming adult squid*, *Journal of Experimental Biology* **208**, 1125 (2005).

35. J. O. Dabiri, S. P. Colin, K. Katija, J. Costello, *A wake-based correlate of swimming performance and foraging behavior in seven co-occurring jellyfish species*, *Journal of Experimental Biology* **213**, 1217 (2010).

36. B. J. Gemmell, *et al.*, *Passive energy recapture in jellyfish contributes to propulsive advantage over other metazoans*, *Proceedings of the National Academy of Sciences* **110**, 17904 (2013).

37. R. Larson, *Cost of transport for the scyphomedusa Stomolophus meleagris L. Agassiz*, *Canadian Journal of Zoology* **65**, 2690 (1987).

38. K. Schmidt-Nielsen, *Locomotion: energy cost of swimming, flying, and running*, *Science* **177**, 222 (1972).

39. A. P. Maertens, M. S. Triantafyllou, D. K. P. Yue, *Efficiency of fish propulsion*, *Bioinspiration & Biomimetics* **10**, 046013 (2015).

40. L. Wen, T. Wang, G. Wu, J. Liang, *Quantitative Thrust Efficiency of a Self-Propulsive Robotic Fish: Experimental Method and Hydrodynamic Investigation*, *IEEE/ASME Transactions on Mechatronics* **18**, 1027 (2013).

41. J. O. Dabiri, *Landmarks and frontiers in biological fluid dynamics*, *Physical Review Fluids* **4**, 110501 (2019).

42. C. Eloy, *Optimal Strouhal number for swimming animals*, *Journal of Fluids and Structures* **30**, 205 (2012).

43. D. Floryan, T. Van Buren, A. J. Smits, *Efficient cruising for swimming and flying animals is dictated by fluid drag*, *Proceedings of the National Academy of Sciences* **115**, 8116 (2018).

44. I. K. Bartol, P. S. Krueger, J. T. Thompson, W. J. Stewart, *Swimming dynamics and propulsive efficiency of squids throughout ontogeny*, *Integrative and Comparative Biology* **48**, 720 (2008).

the paper are present in the paper or the Supplementary Materials. The data for this study have been deposited in the database XXXX.

Supplementary Materials and Methods

Python notebook S1: Cavity geometry calculations. Definition of the cavity geometry and the derivation and calculation of the internal fluid added mass M_{aI} and the geometry scaling factors for the stroke ratio and jet velocity.

Table S2: Constrained free-vibration measurements.

	mean ω_n	std ω_n	mean ζ	std ζ
Air	410 rad/s	9.74 rad/s	-	-
Water	36.0 rad/s	0.450 rad/s	0.148	0.0150

Figure S3: Constrained test image example. These images are used to measure the deflection amplitude and phase of the prototype arms.
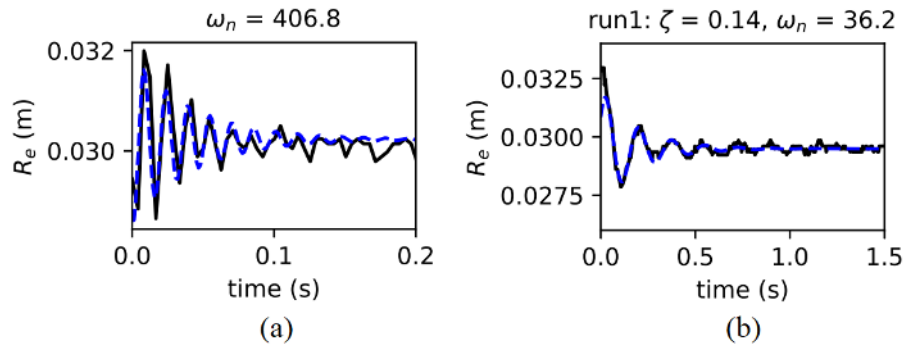
Figure S4: Free vibration example results. Tests in (a) air and (b) water. Black lines are measured motion capture data, blue dashed are the fitted exponentially damped functions used to determine ζ and f_n.
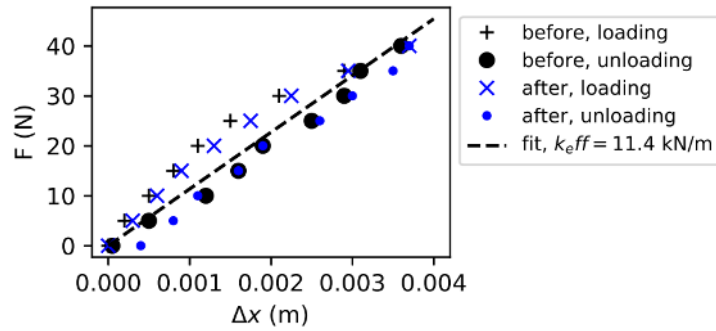

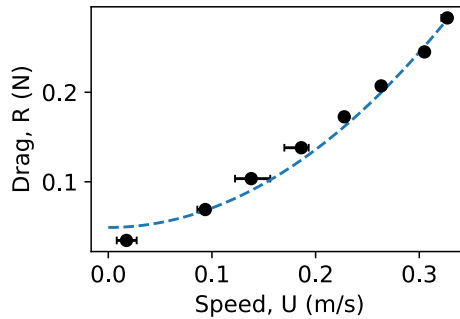Figure S5: Force vs displacement measurements and the linear fit.

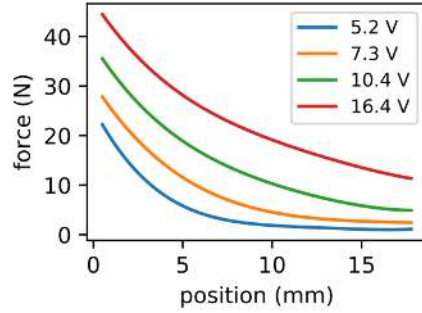Figure S6: Terminal velocity resistance measurements and quadratic fit.

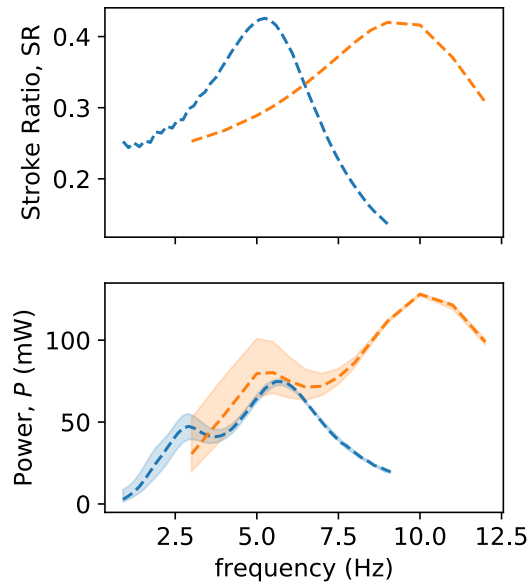Figure S7: Actuator force as a function of relative position and voltage.

Figure S8: Forced oscillator model results. The median and 95% confidence interval predictions of the Stroke Ratio and Power for the constrained (blue) and free swimming (orange) cases. The dynamic model free parameters, the damping ζ and solenoid rest position x_0, have been calibrated against the constrained frequency sweep data in Fig. 4.